RESEARCH ARTICLE

Macromolecular Chemistry and Physics
www.mcp-journal.de

Applying the Inelastic Thermal Spike Model to the Investigation of Damage Induced by High-Energy Ions in Polymers

Maximiliano S. da Rocha, João Pedro M. May, Raquel S. Thomaz, Ricardo M. Papaléo, and Marcel Toulemonde*

This work reports on damage production in polymers by high-energy ions within the framework of the inelastic thermal spike model (i-TS). The model is used to describe the effective size of the damaged region around the ion path (the track size) in amorphous poly(methyl methacrylate) (PMMA) and the semicrystalline poly(p-phenylene sulphide) (PPS), poly(ethylene terephthalate) (PET), and poly(vinylidene difluoride) (PVDF). Track size calculations are compared to experimental data deduced from measurements of crater size, bond-breaking cross-sections, changes in crystallinity and electron density, track etching, and electrical depolarization. The use of data obtained from distinct types of damage provides a broad platform to test the applicability of the model to polymers. This work shows that the i-TS correctly describes the dependence of the track size on energy loss obtained from most experimental probes, when the activation energy of thermal decomposition of the polymers is used as the criterion of track formation, using an electron–phonon mean free path of ≈3 nm. As damage is not uniform across the ion track radial dimension, there are fine variations in the experimental damage radii that can only be accounted for by using multiple activation processes. Amorphization radii of the semicrystalline polymers are not directly correlated to melting induced by the ions.

1. Introduction

Polymers and other organic compounds are very sensitive materials to ionizing radiation, degrading easily at relatively small exposure doses.[1,2] When irradiated with swift heavy ions, where high levels of local energy transfer are involved, individual ions produce nanometer-sized trails of damaged material known as ion tracks.[3,4] Inside the material, ion tracks are seen as micrometer-long quasi-cylindrical structures with a well-defined track radius usually in the order of 5–10 nm. At the polymer surface, ion tracks appear in the form of craters which may be surrounded by ridges.[5,6] Crater volumes measured by AFM (≈400 nm^3 for a 1 GeV Au in poly(methyl methacrylate) (PMMA)) correspond to a displaced mass of about 10^5–10^6 u. Ion tracks may also be selectively developed by means of chemical etching to produce nano- and micropores.[3,4] Track-etched membranes are routinely used in commercial filters, and as templates to produce various kinds of nano- and microstructures. A variety of sophisticated applications of etched ion tracks has been envisaged.[7,8] The understanding of ion track formation and how track size depends on the ion energy loss and on the properties of the target materials are fundamental issues underlying most of the phenomena induced by swift heavy ions in organic matter and the applications derived from them.

Experimentally measured track sizes are not unique but probe-dependent, because different techniques probe different types of damage or material modification. Transmission electron microscopy (TEM), the most common method applied to the investigation of track size in crystalline inorganic materials,[9] gives the amorphization or phase change radius.[10] Small angle x-rays scattering (SAXS)[11] is sensitive to electron density changes. Calorimetric measurements and X-ray diffraction (XRD) probe crystallinity changes,[12] and vibrational spectroscopy,[13–16] and ion track etching[17] are sensitive to chemical damage (bond-breaking). Each technique may give an effective track radius, which can vary significantly. For polymers, it is usually difficult to extract track radii directly from TEM observations.[18] Thus, most of the available experimental data have been deduced from ion track etching, scanning force microscopy, SAXS, XRD, and infrared spectroscopy.

M. S. da Rocha, J. P. M. May, R. S. Thomaz, R. M. Papaléo
Interdisciplinary Center of Nanoscience and Micro-NanoTechnology
School of Technology
Pontifical Catholic University of Rio Grande do Sul
Porto Alegre, RS 90619-900, Brazil
E-mail: papaleo@pucrs.br

R. S. Thomaz
Ion Implantation Laboratory
Federal University of Rio Grande do Sul
Porto Alegre, RS 90040-060, Brazil

M. Toulemonde
Centre de Recherche sur les Ions, les Matériaux et la Photonique
CEA-CNRS-ENSICAEN-Université de Caen
CIMAP-GANIL Bd. H. Becquerel CS 65133, Caen cedex 5 14076, France

The ORCID identification number(s) for the author(s) of this article can be found under https://doi.org/10.1002/macp.202200339

DOI: 10.1002/macp.202200339

Different models have been proposed to explain ion track formation and predict track-size in materials. This includes the Coulomb Explosion model,[3] the bond weakening model,[19] the self-trapped exciton model,[20] and different versions of thermal spike models.[21] Due to the complexity of modeling macromolecules and the difficulties of finding appropriate input parameters for polymeric materials, only a limited number of theoretical investigations has been performed so far for this class of material. One example is the analytical thermal spike (a-TS),[22] which was applied to describe ion tracks in PET).[23] In this model, it is assumed that a fraction f of the initial deposited energy in the electrons is transferred to the lattice, giving rise to a gaussian temperature increase ΔT(r,t) as a solution of the heat diffusion equation in the atoms. The initial width of the temperature profile is assumed to be dependent of the ion velocity and together with f are used as two free parameters. Track size is then related to the region where ΔT(r,t) surpasses a critical temperature such as the melting temperature, neglecting the energy necessary to induce the phase change.[22,23]

In the present paper, we analyze ion track production in polymers within the framework of the inelastic thermal spike model (i-TS).[21,24–26] In this model, the heat diffusion in the electron and lattice subsystems are coupled and calculated numerically, assuming that the energy deposited by a swift heavy ion can be thermalized on the electrons and then transferred to the atoms by the electron–phonon coupling. Differently from the a-TS model, the energy necessary to make a phase change, e.g., melting or vaporization is also considered. Moreover, in the i-TS model the total electronic energy loss is used in the calculation of the energy transferred to the lattice, instead of an arbitrary conversion factor f. In this description, there is only one free parameter: the electron–phonon mean free path. The i-TS model has been successfully applied to describe track size as a function of the electronic energy loss in different materials, such as metals,[27,28] inorganic insulators,[24–26,29–31] and semiconductors,[32–34] using the energy to melt or vaporize as the criteria for track formation. For polymers, one preliminary investigation was conducted to describe ion track etching in polyimide.[35]

Here, the i-TS model is used to calculate the track size in a broad range of ion energies in four polymers: the amorphous PMMA and the semi-crystalline poly(p-phenylene sulphide) (PPS), poly(ethylene terephthalate) (PET), and poly(vinylidene difluoride) (PVDF). The calculated track radii are compared to experimentally measured track sizes deduced from: a) crater diameter induced by individual ion impacts in PMMA,[5,36,37] b) bond breaking cross-sections derived from infrared absorption spectroscopy (IRAS) in the case of PET[14,15] and PPS,[13] c) track radii deduced from etching experiments in PET,[17] and d) depolarization measurements[38] and structural changes observed by XRD[12] and by SAXS[39] in the case of PVDF. The use of data obtained from experimental techniques that probe different types of damage provides a broad platform to test the applicability of the inelastic thermal spike model to the investigation of ion tracks in polymers.

We show that the radius in the thermal spike where enough energy is given for thermal decomposition of the polymers compares reasonably well to the track size extracted from several experimental probes in a wide range of energy loss. Only depolarization of β- PVDF correlates clearly with the size of a molten zone. This is distinctly different from what is observed for other inorganic insulators and metals, where the appearance of a melt phase is the dominant criterion of track formation.

2. Implementation of the Inelastic Thermal Spike Calculations

2.1. Model Description

The inelastic thermal spike (i-TS) model[24] was developed to determine quantitatively the track radii in the electronic energy loss regime and was applied for numerous insulators.[25] It describes how the ion energy, initially deposited on the electrons, diffuses (within the electron subsystem) before it is transferred to the lattice atoms. In the model, two coupled differential equations govern the heat diffusion and energy exchange in the electronic and atomic subsystems:

$$C_e\left(T_e\right)\ \frac{\partial T_e}{\partial t} = \frac{1}{r}\ \frac{\partial}{\partial r}\left[rK_e\left(T_e\right)\frac{\partial T_e}{\partial r}\right] - g\left(T_e - T_a\right) + A\left(r\left[\nu\right], t\right) \tag{1}$$

$$C_a\left(T_a\right)\ \frac{\partial T_a}{\partial t} = \frac{1}{r}\ \frac{\partial}{\partial r}\left[rK_a\left(T_a\right)\frac{\partial T_a}{\partial r}\right] + g\left(T_e - T_a\right) \tag{2}$$

where t is the time; r is the radial distance from the ion path axis; and $T_{e,a}$, $C_{e,a}$, and $K_{e,a}$ are the temperature, the specific heat, and the thermal conductivity of the electronic and atomic subsystems, respectively. $A(r[\nu],t)$ is the initial energy distribution on the electrons. The electron–phonon coupling g is the only free parameter. Equations (1) and (2) are solved numerically, assuming cylindrical geometry, giving $T_a(r,t)$, from which track radii are extracted based on a given physical criterion. For details of the model described elsewhere.[21] Due to the rapid heating of the atoms, the temperature calculations do not stop at the melting temperature or vaporization temperature. This was shown experimentally[40] and described theoretically.[41] Thus, above the melting temperature it is the superheating temperature that is calculated and reported.

2.2. Initial Distribution of Deposited Energy, Electron–Phonon Mean Free Path, and Thermodynamic Parameters for the Electronic Subsystem

The initial energy distribution on the electrons ($A(r[\nu],t)$), which is dependent on the ion velocity (ν), is deduced from Monte–Carlo calculations that compute numerically the development of the electrons cascades induced by the primary ions.[42] Integration of $A(r[\nu],t)$ over time and space is equal to the corresponding electronic energy loss as calculated by SRIM.[43] As an example, typical radial energy distributions in PVDF due to secondary electrons are plotted in **Figure 1**, in the form of accumulated deposited energy as a function of radial distance from the track center. From these curves, a radius (R_e) in which 66% of initial energy is deposited on the electrons is defined. Such radius increases with ion specific energy (dashed line in Figure 1a) and depends

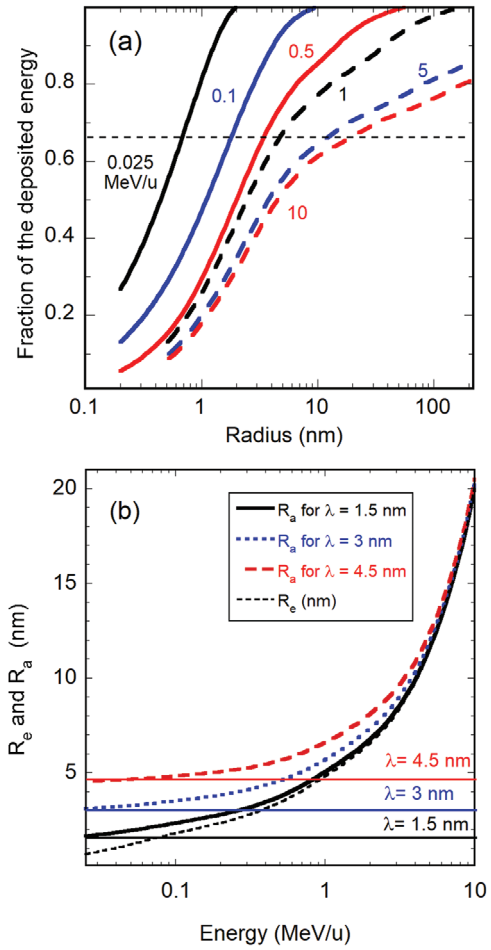

Figure 1. a) Fraction of energy deposited on the electrons in poly(vinylidene difluoride) (PVDF) as a function of the radial distance from the ion axis for various ion velocities (in MeV u^{-1}). The horizontal dashed line indicates the 66% level. b) Mean absorption radii R_e and R_a in which 66% of electronic energy is deposited in the electrons (R_e) or in the atoms (R_a) as a function of beam energy for three values of the electron–phonon mean free path λ.

on the type of material,[25] but it is not much different among the polymers investigated in this work.

The electron–phonon coupling g, the only free parameter in the model, is linked to the electron–phonon mean free path λ, or to the electron–phonon mean free time τ through the relations $g = K_e(T_e)/\lambda^2$ and $g = C_e(T_e)/\tau$.[24,25] For the high electronic temperatures involved, K_e and C_e can be assumed to be constant with $K_e(T_e) = 2$ J cm^{-1} s^{-1} K^{-1} and $C_e(T_e) = 1$ J cm^{-3} K (as for most insulators[24,25]). The two parameters λ and τ define, respectively, the mean free path length and the mean free time of energy diffusion on the electrons before it is transferred to the lattice. They are linked via the relation $\tau = C_e(T_e)\ \lambda^2/K_e(T_e) = \lambda^2/2$.

The λ values have been deduced from a systematic study of track formation in amorphisable crystalline insulators and follow a monotonic decrease with increasing optical band gap.[24,25] Based on this trend and using the reported band gaps of 6.2 eV for crystalline PVDF,[44] ≈4 eV for PMMA[45] and PET,[46] and ≈3 eV for PPS,[47] λ should be around 4.5 nm for these polymers. However, λ values were also found to decrease in disordered or defective materials.[21] Hence, as commercial PVDF, PET, and PPS are semicrystalline (crystallinity at most 50%) and PMMA is amorphous, the λ values for these polymers may be smaller than what is expected based on the band-gap empirical rule. Consequently, in the calculations λ was varied between 2 and 5 nm to encompass such possible variations.

This λ range can be compared to the electron energy deposition radius R_e (Figure 1b). If $\lambda >> R_e$, i.e., for low ion velocities, the electron–phonon mean free path will define the initial volume in which the energy is transferred from the electrons to the lattice. On the other hand, if $\lambda << R_e$, i.e., for fast ions, it is R_e, that will govern the effective volume of energy transfer. To be more quantitative, a cylinder radius R_a can be defined to parametrize the effective initial volume of excited lattice atoms, which is assumed to be a quadratic combination of λ and R_e ($R_a^2 = \lambda^2 + R_e^2$).[25] R_a is plotted in Figure 1b for PVDF, using λ values between 1.5 and 4.5 nm. It is clear from this figure that when the beam energy is larger than about 4 MeV u^{-1}, λ has little effect on the initial volume in which the energy is transferred to the atoms. On the other hand, the choice of λ is of great significance for ions at low specific energies. greater than 3 MeV u^{-1}.

2.3. Thermodynamic Parameters for the Atomic Subsystem of the Polymers

We have used experimental data from four polymers: PMMA, $[C_5H_8O_2]_n$); PPS($[C_6H_4S]_n$); polyethylene terephthalate (PET, $[C_{10}H_8O_4]_n$); and PVDF ($[C_2H_2F_2]_n$). The thermodynamic parameters needed for the lattice subsystem are specific for each polymer and were taken from tabulated values from the literature.[48–57] Tables S1 and S2 (Supporting Information) present several lattice properties (thermal conductivity, specific heat, melting temperature, thermal degradation temperature) of PMMA, PVDF, PPS, and PET extracted from distinct sources. As usual for polymeric materials, the reported values vary somewhat, depending on the manufacturer. The variability of tabulated data derives mainly from the distinct processing conditions among different brands, the possible presence of additives or stabilizers, and variations in molecular weight distribution, molecular orientation, and index of crystallinity. Several calculations were performed varying the input parameters within the ranges found in the literature to evaluate how much they affect the calculated track radii. The differences found are typically smaller than the error in the experimentally measured values. Consequently, we selected for the i-TS calculations only one set of parameters (also quoted in Tables S1 and S2, Supporting Information) based on polymer specifications that were closest to the one employed in the experiments. The selected data for PVDF were calorimetric measurements from the work of dos Santos et al.[48] and Botelho et al.[49] Regarding PMMA, we used the curve of specific heat as a function of the temperature shown in the thesis of Steinhaus[50] and a recent work of Korobeinichev et al.[51] about the kinetics of thermal decomposition of PMMA. For PPS, we used technical information directly provided by the manufacturer (Toray[52]) and data from pyrolysis kinetics.[53] Regarding PET, calorimetric measurements from Minakov et al.[54] and thermal degradation data by Das and Tiwari[55] were employed.

The curves of specific heat of PVDF, PMMA, PPS, and PET, as a function of temperature are provided in Figure S1 (Supporting Information). By integration of the specific heat curves, the energy at the molten state (E_m) is determined to be equal to 564.23 J g^{-1} or 0.062 eV at^{-1} for PVDF. A similar procedure was applied to the other semicrystalline polymers, and the results are given in Section 3. PMMA samples in the experiments are amorphous and do not undergo a melting phase transition. Nevertheless, for the sake of the calculations, the energy per atom needed to melt PMMA was assumed to correspond to the integration of the specific heat curve up to the melting temperature of crystalline PMMA (433 K). In this way, the energy per atom at the melting temperature of PMMA results in 487.4 J g^{-1} (or ≈0.034 eV at^{-1}).

Polymers usually degrade before vaporizing, thus we used thermal degradation temperatures to estimate the energy needed to put molecules in the gas phase, instead of a vaporization process. Tabulated thermal degradation temperatures also vary somehow, depending on the processing conditions (Tables S1 and S2, Supporting Information). For PVDF, the activation energy used was 100 kJ mol^{-1},[49] which is equivalent to ≈1562 J g^{-1}, or ≈0.173 eV at^{-1}. For PMMA the thermal decomposition activation energies ranged from 150.5 to 188.8 kJ mol^{-1},[51] or 0.104 to 0.130 eV at^{-1}. Here, 0.125 eV at^{-1} was used as the reference. For PPS and PET, the activation energies used were 170[53] and 355 kJ mol^{-1},[55] which correspond to 0.185 and 0.167 eV at^{-1}, respectively.

The thermal conductivity K_a of the investigated polymers has a weak dependence on the temperature. For the calculations in this work, we used the mean between the reported maximum and minimum values of the thermal conductivity (0.00225 W cm^{-1} K^{-1} for PVDF[48]; 0.00194 W cm^{-1} K^{-1} for PMMA[50]; 0.0029 W cm^{-1} K^{-1} for PPS Torelina[56]; and 0.0013 W cm^{-1} K^{-1} for Hostaphan PET[57]).

2.4. Calculation of the Energy Distribution and Evolution in the Lattice

Typical results of the numerical calculations of the two coupled equations performed for PVDF using $\lambda = 3$ nm for an ion with an electronic energy loss of 12 keV nm^{-1} and energy of 5 MeV u^{-1} are presented in **Figure 2**. In the figure, the electron temperature, the lattice superheating temperature, and the deposited energy on the atoms are plotted as a function of time for different radial distances from the ion path. Figure 2a shows the temporal evolution of the electronic temperature. The electrons are cooled down in about 10^{-12} s, what is expected because for a λ of 3 nm the electron–phonon mean free time is $\tau = 2 \times 10^{-13}$ s. As the cooling of the atomic system is relatively slow due to the very low lattice thermal conductivity, the calculations were extended up to 2×10^{-9} s to allow cooling down of the molten phase. The total energy needed for melting and to thermally decompose PVDF, and the corresponding superheating temperatures of melting (T_{sm}) and of thermal degradation (T_{sd}) are marked as horizontal dashed lines in Figure 2b,c. These parameters are used to derive the radii where the ions induce melting and thermal decomposition of the material. As an example, in Figure 2, the maximum radial extent of the molten zone is about 15 nm. Thermal decomposition of PVDF appears across a radius of about 5.5 nm around the track center. The cooling times to reach energy levels in the lattice around E_d and E_m are equal to 3×10^{-10} and 2×10^{-9} s, respectively.

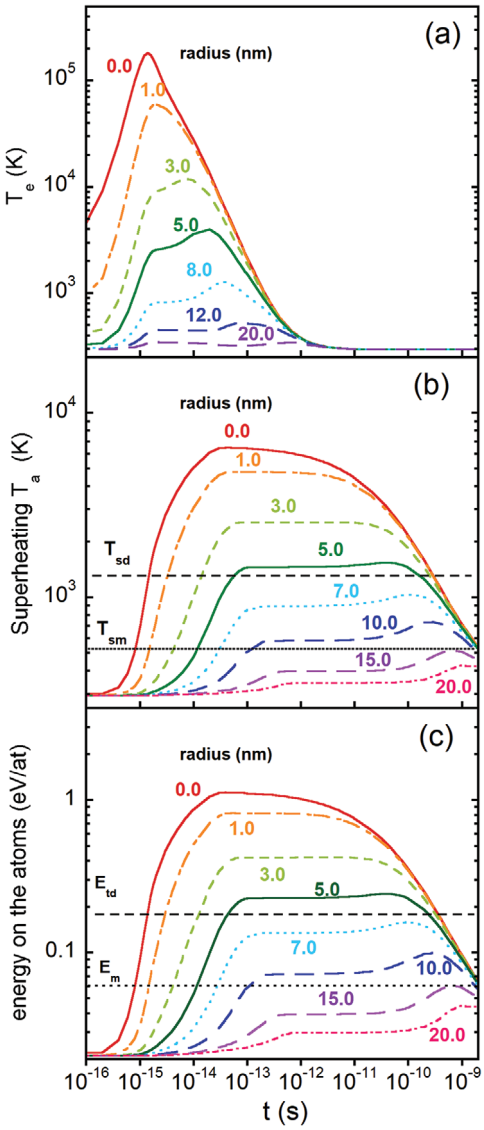

Figure 2. a) Electronic temperature, b) superheating atomic temperature, and c) energy deposited on the atoms as a function of time in poly(vinylidene difluoride) (PVDF) irradiated by 5 MeV u^{-1} ions with $(dE/dx)_e$ of 12 keV nm^{-1} and $\lambda = 3$ nm. The results are shown at various radial distances from the ion path. The horizontal lines in (b) and (c) show the energy level at E_m and E_d (atomic energy for melting and thermal decomposition, respectively) and the corresponding superheating temperatures T_{sm} and T_{sd} for the appearance of a molten phase and for the material thermal decomposition.

3. Track Radii and Comparison with Experimental Data

Experimental data used here give the effective modification radii as a function of electronic energy loss in the range between 0.5 and 24 keV nm^{-1}. Some of these data were collected using ions

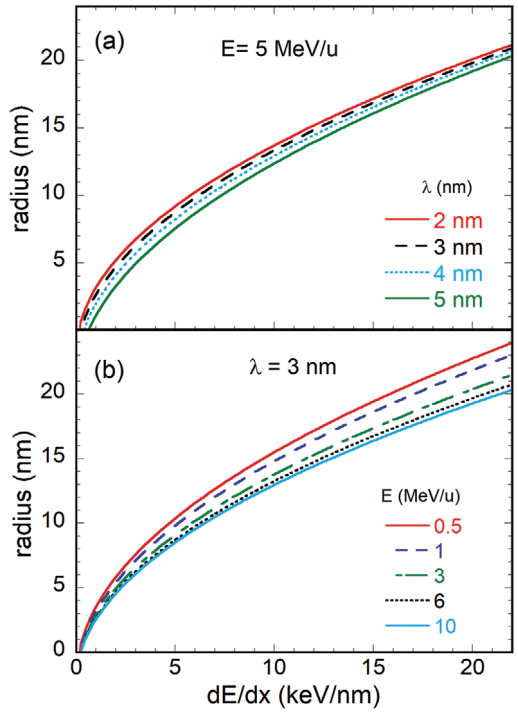

Figure 3. Radius of the molten zone (E_m = 0.062 eV at^{-1}) as a function of energy loss in poly(vinylidene difluoride) (PVDF) a) for different values of λ at a fix velocity of 5 MeV u^{-1} and b) for various ion velocities and λ = 3 nm.

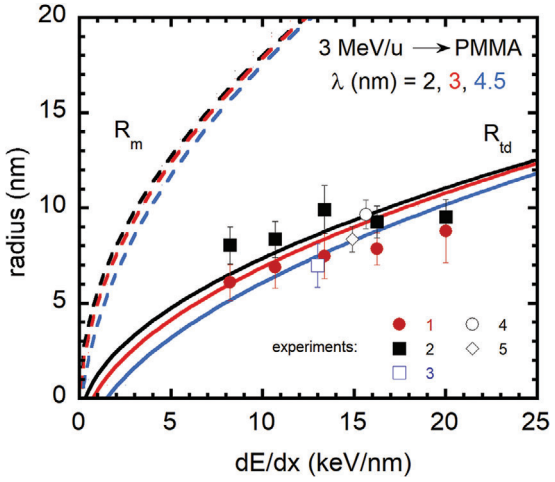

Figure 4. Radii of melting R_m (dashed lines) and thermal decomposition R_{td} (solid lines) induced in poly(methyl methacrylate) (PMMA) as a function of energy loss at a fixed specific energy of 3 MeV u^{-1} derived from i-TS calculations. Activation energies of thermal decomposition of 0.125 eV at^{-1} and of melting of 0.034 eV at^{-1} were used. Curves for electron–phonon mean free path λ varying from 2 to 4.5 nm are shown. Symbols are experimental data of crater radii induced in PMMA films deposited on Si wafers under different experimental conditions: (1) 3 MeV u^{-1} Au^{q+} on 105 nm-thick films prepared with 159 000 u PMMA,[5] (2) 3 MeV u^{-1} Au^{q+} on 10 nm-thick films, M_w = 950 000 u,[5] (3) 11.1 MeV u^{-1} Au on 13 nm-thick films, M_w = 370000 u,[36] (4) 4.8 MeV u^{-1} Pb, 43 nm-thick films, M_w = 370 000 u[36]; (5) 5.6 MeV u^{-1} Au on 40 nm-thick films, M_w = 130 000 u.[37]

covering a broad range of velocities (specific energies lying between 0.6 to 11.4 MeV u^{-1}). This means that velocity effects may not be negligible. Thus, initially, calculations have been performed to verify how much the beam specific energy and the value of the electron–phonon mean free path influence the extracted track radii. This is presented in **Figure 3**, using PVDF as a reference, but trends are similar for the other polymers. In Figure 3, track radii correspond to the size of the excited region in the polymer where the deposited energy E on the atoms reached levels equivalent to the energy of melting (i.e, the maximum radial distances from the track center where $E \geq E_m$). For beams with specific energy of 5 MeV u^{-1}, the variation of the track radii as a result of changes in λ from 2 to 5 nm is within ±15% at 4 keV nm^{-1} and only within ± 5% at 24 keV nm^{-1}. Regarding the effect of ion velocity (Figure 3b, λ = 3 nm), when the beam specific energy increases from 0.5 to 10 MeV u^{-1} the radius varies ±15% at 4 keV nm^{-1} and ±10% at 20 keV nm^{-1}. Thus, the variation of the calculated radii is within the error of the experimentally measured values, which is typically at least ± 15%. Indeed, in several data sets used here, changes in track size due to ion velocity are small compared to the error bars. Thus, when the experimental data were obtained using beams of different specific energies, the average specific energy of the set was used in the calculations.

3.1. PMMA

Figure 4 shows data for a series of experiments on cratering induced by individual ion impacts on amorphous poly(methyl methacrylate). In one set of measurements, craters were produced by charge-state selected Au ions at 3 MeV u^{-1} (Au^{q+}, 30 < q < 51). This was performed in thick and thin films of PMMA with different molar masses (from 130 000 up to 950 000 u).[5] They are an interesting (and rare) set of data where dE/dx is varied keeping ion velocity and atomic number constant. Some additional cratering experiments obtained with swift heavy ions of different velocities (4.8 MeV u^{-1} Pb; 5.6 MeV u^{-1} Au, and 11.1 MeV u^{-1} Au) but similar dE/dx[36,37] are also included in the figure for comparison. In all such experiments, crater diameters at the surface were directly extracted from scanning force microscopy (SFM) measurements and are converted into a track radius in Figure 4. The interpretation of this radius is direct. It corresponds to the maximum lateral size where material erosion occurs and is closely related to sputtering and thermal decomposition of the polymer into the gas phase.

In Figure 4, i-TS results from calculations of the track size as a function of energy loss at a fixed velocity of 3 MeV u^{-1} are also displayed for three values of the electron–phonon mean free path λ (2, 3, and 4.5 nm). Dashed lines correspond to the maximum radii of melting R_m (assuming energy at the molten state of 0.034 eV at^{-1}) and of thermal decomposition R_{td} (activation energy of thermal decomposition of 0.125 eV at^{-1}). Very good agreement is obtained between experimental crater size and the calculated thermal decomposition radii. Saturation at high energy losses, however, appears to be more pronounced in the experiments than in the model predictions. Considering the data scatter and the slightly different scaling of track radii versus energy loss seen in the experiments and calculations, an electron–phonon mean free

path of $\lambda = 3 \pm 1$ nm can be imputed for PMMA. Considering the band gap energy of ≈4 eV of PMMA and the fact that it is an amorphous material, a λ smaller than 4.5 nm would be expected. Thus, the activation energy for thermal degradation appears to be an adequate parameter to describe crater size in PMMA, using an electron–phonon mean free path close to 3 nm.

3.2. PPS

For PPS, track radii extracted from spectroscopy studies of bond breaking were used[13] to compare to i-TS calculations. Such experiments were performed on Torelina foils irradiated by a series of ions from 2.46 MeV He to 78.2 MeV I, all with a fixed specific energy of 0.61 MeV u^{-1}. Bond breaking cross-sections σ_b were derived from exponential fittings of the curves of the intensity of infrared bands (area of the peaks) as a function of irradiation fluence ϕ : $A(\phi) = A_0 \exp(-\sigma_b \phi)$. This is the expected law when each impinging ion destroys a certain chemical bond inside an effective cylinder of cross-sectional area σ_b (around the ion path) and length equal to the sample thickness, and overlapping damaged areas produce no further effect.[13] Effective track radii can then be extracted assuming cylindrical geometry and $R_b = (\sigma_b/\pi)^{1/2}$. Several bonds were followed, including C–S, S–S, C–C, and C–H. When distinct IR bands overlap, the individual peak areas are obtained from deconvolution procedures, using the software of the equipment.

In **Figure 5**, the bond breaking radii obtained from six vibrational bands is plotted as a function of energy loss, together with calculations from the i-TS model using different values of λ (2, 3, and 4.5 nm). For the calculations, the specific energy was set at 0.61 MeV u^{-1}, and the thermodynamic parameters to obtain the melting and thermal decomposition radii were $E_m = 0.040$ eV at^{-1} and $E_{td} = 0.185$ eV at^{-1} (see Tables S1 and S2, Supporting Information). Again, as in the case of cratering in PMMA, using thermal decomposition as the physical criterion of track formation provides a very good match between experimental and calculated track sizes.

We note however, that the use of a single activation energy cannot describe the systematic variations in the bond breaking cross-sections with the type of chemical bond seen in the experiments. It is well-known in irradiated organic materials that the weakest bonds in the chain show the largest cross-sections,[2,13,16,17,19] as it is seen in Figure 5. The most sensitive S–S and C–S bonds assigned to the bands at 480 and 554 cm^{-1}, respectively, have larger damage cross-sections, as compared to C–C bonds (bands at, e.g., 1392 or 1473 cm^{-1}). Because C–C bond breaking cross-section is a marker of the size of the region around the ion path where strong chemical modification or carbonization of the polymer occurs, track radii derived from them shall be closely related to thermal decomposition. Based on that, we use the C–C cross-section data and the thermal decomposition activation energy of PPS to estimate λ for this polymer, resulting in a value of (3.2 ± 0.3) nm. The fact that C–S and S–S have larger effective radii is associated to the smaller activation energies for breaking such bonds. This is explored in Figure 5b where the curves of damage radii as a function of dE/dx are replotted using a single $\lambda = 3.2$ nm and activation energies of 0.135 eV at^{-1} for S–S bonds and 0.185 eV at^{-1} (i.e., E_{td}) for the C–C bonds.

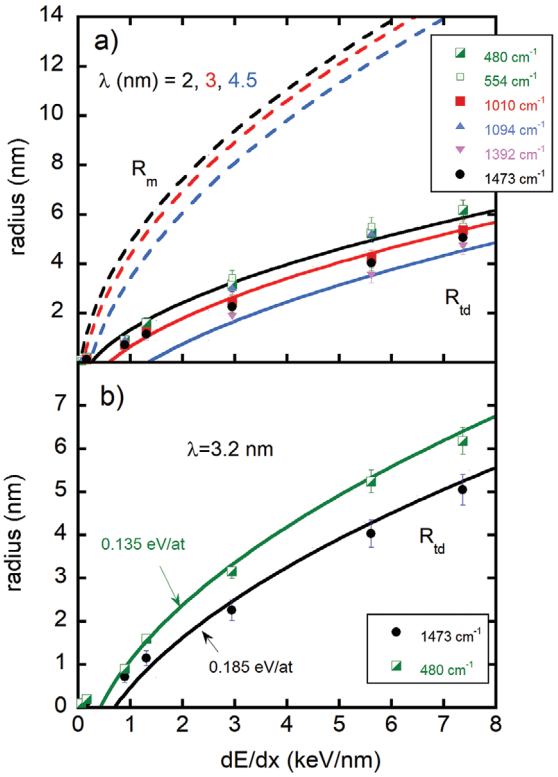

Figure 5. a) Radii of melting R_m (dashed lines) and thermal decomposition R_{td} (solid lines) induced in poly(p-phenylene sulphide) (PPS) as a function of energy loss at a fixed specific energy of 0.61 MeV u^{-1} derived from i-TS calculations. Activation energies of thermal decomposition of 0.185 eV at^{-1} and of melting of 0.040 eV at^{-1} were used. Curves for electron–phonon mean free path λ varying from 2 to 4.5 nm are shown. Symbols are experimental data of effective bond-breaking radii induced in PPS foils for different bonds: S–S (480 cm^{-1}); phenyl ring-S (554 cm^{-1}); C=C (1010 cm^{-1}); C–S (1094 cm^{-1}); C–C (1392 cm^{-1}); C–C (1473 cm^{-1})[13]. b) Zoomed view showing the data for the bands at 480 and 1473 cm^{-1} and the calculated R_{td}. For the C–C band the activation energy of thermal decomposition is used to derive the optimum electron phonon mean free path which is $\lambda = 3.2 \pm 0.3$ nm. Using this λ, an activation energy of 0.135 eV at^{-1} is extracted for S–S bonds.

As the data of PPS were taken at constant ion velocity and at relatively low dE/dx they allow a more precise analysis at the threshold region. Melting and thermal decomposition radii from i-TS always show a threshold dE/dx, while for the experimental radii derived from damage cross-sections no clear threshold is seen. This suggests that at very low energy loss, when the density of ionization is small, damage cannot be ascribed to pyrolysis along a continuous track, but mostly to single electronic excitations. Thermal spikes are supposed to emerge under conditions of dense electronic excitation, usually seen only in the wake of swift heavy ions. Thus, it is not surprising that the low dE/dx points in the PPS cross-section data deduced from irradiations with, e.g., He ions do not follow the threshold regime of i-TS.

3.3. PET

Four sets of track size measurements in PET have been used for comparison with the i-TS calculations. Each one was acquired

using a different technique (IRAS, SAXS, XRD, and chemical etching) and are discussed separately.

Damage cross-sections derived from infrared absorption spectroscopy data were extracted from the work of Zhu et al.[14,15] They have irradiated commercial 15 µm-thick PET foils (crystallinity around 42%) with high energy heavy ions (from 11.4 up to 35 MeV u^{-1}) with several fluences and also used the Poisson law to obtain the damage cross-sections as in the case of PPS discussed above. They in addition used foil stacking to degrade ion energy and irradiate samples in a broader range of energy loss. In **Figure 6**a, effective damage radii for bond breaking $R_b = (\sigma_b/\pi)^{1/2}$ are plotted as a function of energy loss for the bands at 973, 1506, and 3299 cm^{-1} together with the track radii calculated using the i-TS model. For the i-TS calculations, a specific energy of 5 MeV u^{-1} was used with λ values between 2 and 4.5 nm. The radii of melting (with $E_m = 0.064$ eV at^{-1}) are shown as dashed lines and the thermal decomposition radii (with an activation energy of E_{td} = 0.167 eV at^{-1}), as solid lines.

The band at 3299 cm^{-1} is not related to destruction, but to production of alkyne end groups (–C≡C–H). The production of carbon triple bonds requires a huge reorganization of the bonds and large ionization densities in the track. The band shown at 973 cm^{-1} is assigned to the ethylene glycol residue of PET and is sensitive to conformational order (and thus crystallinity). Radii extracted for these bands follow closely the curve of R_{td} for λ around 3 nm. Similarly, to the case of PPS, λ around 3 nm and thermal decomposition are adequate choices to reproduce experimental ion track sizes derived from vibrational spectroscopy. However, as the uncertainties in both the experimental cross-sections and in the ion energy (or energy loss) are relatively large, the PET data are not very suitable for a fine selection of the electron phonon mean free path or for extraction of bond breaking activation energies.

The cross-sections of the band at 1506 cm^{-1} (attributed to the phenyl ring) are significantly smaller than the other IR bands. It is striking that two bands clearly associated to the carbonization of the chains (1506 and 3299 cm^{-1}) have such distinct behavior. It is unclear whether such discrepancies result from uncertainties of peak area determination in the IR spectra (a common drawback in IRAS analysis of weak and overlapping bands) or reflect an actual difference in sensitivity of the bonds. In addition, radii extracted from SAXS measurements of PET-Hostaphan irradiated by 11.4 MeV u^{-1} ions[39] (also shown in Figure 6a) are comparable to those of the 1506 cm^{-1} band and also systematically smaller than thermal decomposition radii calculated from the i-TS model. Radii derived from SAXS reflect the decrease in density along the track, which for polymers is associated to pyrolysis and the emission of volatiles. By fitting the SAXS radii, an activation energy of ≈0.3 ± 0.5 eV at^{-1} is extracted, which is much larger than the activation energy of thermal decomposition of PET (0.167 eV at^{-1}) reported in the literature.

Next, we compare the calculations with data on track size derived from chemical etching experiments obtained from commercial PET foils (Hostaphan and a Russian brand, crystallinity ≈40%). In this case, very low fluences were employed, using beams of different ion velocities and in an energy loss range between 3 and 24 keV nm^{-1} at. The authors defined the track size as the point where the etching rate is a minimum. The minimum of the etch rate occurs when the etchant encounters a highly

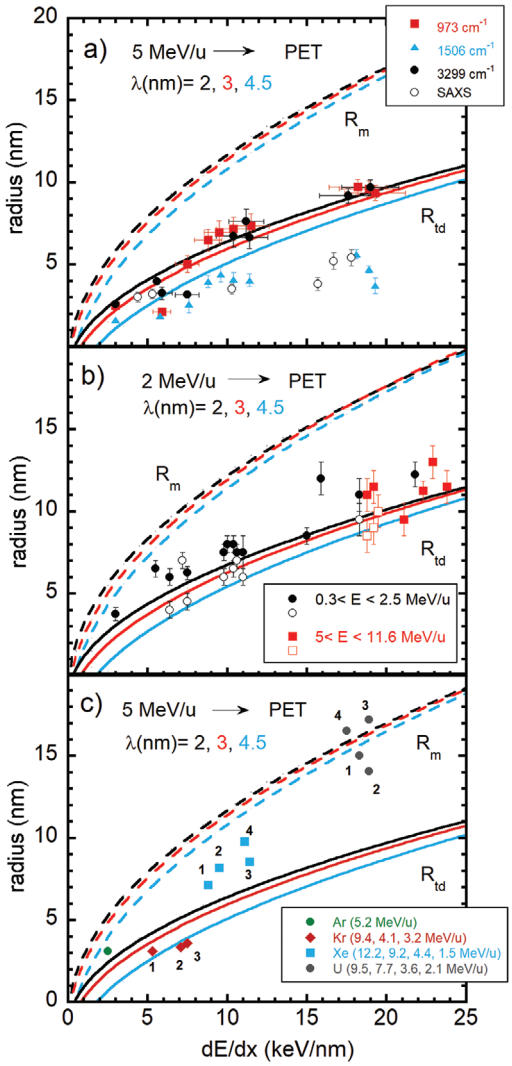

Figure 6. Comparison between track radii measured in poly(ethylene terephthalate) (PET) (symbols) and radii of melting R_m (dashed lines) and thermal decomposition R_{td} (solid lines) as a function of energy loss. In the i-TS calculations, activation energies of thermal decomposition of 0.167 eV at^{-1} and of melting of 0.064 eV at^{-1} were used, varying λ from 2 to 4.5 nm. a) A specific energy of 5 MeV u^{-1} was used in the calculations to compare to track size derived from bond breaking cross-sections induced by beams of various specific energies[14,15] (most of the data between 2 and 8 MeV u^{-1}). Small angle X-rays scattering (SAXS) data at 11.4 MeV u^{-1}[39] were also included. b) A specific energy of 2 MeV u^{-1} was used in the calculations to compare to experimental data of track size derived from chemical etching in a broad range of ion velocities (black symbols indicate ions with 0.3 to 2.5 MeV u^{-1}; red symbols, 5 to 11.6 MeV u^{-1}).[17,58] Open and filled symbols indicate the use of the etchants 1 M K_2CO_3 and 0.1 N NaOH, respectively. c) A specific energy of 5 MeV u^{-1} was used in the calculations to compare to amorphization radii extracted from X-ray diffraction (XRD) data in a broad range of ion velocities.[15] The numbers indicate the ion velocity from high to low, 1 being the highest value.

cross-linked region around the track core[17,58]. The radii obtained through this procedure are shown in Figure 6b. Here, in order to assist in the analysis, the data were grouped in two classes: high velocity (5–11.6 MeV u^{-1}) and low velocity (below 2.5 MeV u^{-1}) ions. Other beam energies were also obtained from foil stacking.

These data are compared to track radii of melting and thermal decomposition calculated from the i-TS model with similar parameters as in Figure 6a. The beam specific energy was set at 2 MeV u^{-1} to represent the experimental condition of the low velocity ions. One can see that, for this set of results, velocity effects are negligible as the high velocity points (red symbols in Figure 6a) are comparable to those obtained at low velocities. Scattering in the data is relatively large (in part associated with distinct etching conditions). Nevertheless, the criterion of thermal decomposition is the one that produced the best agreement with the experimental points in all the dE/dx range, although in several cases track radii derived from i-TS are systematically smaller. Moreover, effective radii derived from etching follow nearly the track radius deduced from FTIR spectroscopy for the 973 and 3299 cm^{-1} bonds.

Finally, in Figure 6c, effective amorphization radii derived from XRD measurements of 15 µm-thick commercial PET foils are presented. Amorphization cross-sections were extracted from the decay of the (100) peak area of the PET diffractogram.[15] Data are again compared to the i-TS results, using the same parameters as above. It is interesting to note that the amorphization radii in PET have a different (steeper) dE/dx dependence than bond breaking cross-sections or radii derived from etching experiments. At low dE/dx, amorphization and bond-breaking (destruction of the transconfiguration of the ethylene glycol residue at 973 cm^{-1}) have comparable cross-sections, i.e., amorphization appears to be closely connected to the change in trans to gauche conformation in the PET chains. However, at high dE/dx amorphization radii are much larger than bond-breaking and approach the melt radii R_m derived from i-TS. It is intriguing that in the low dE/dx regime infrared and XRD signals obtained by Zhu and collaborators[15] decay at a similar rate. In a previous work on PET foils (Mylar) bombarded by low energy ions, amorphization radii deduced from XRD were clearly larger than bond-breaking radii.[59]

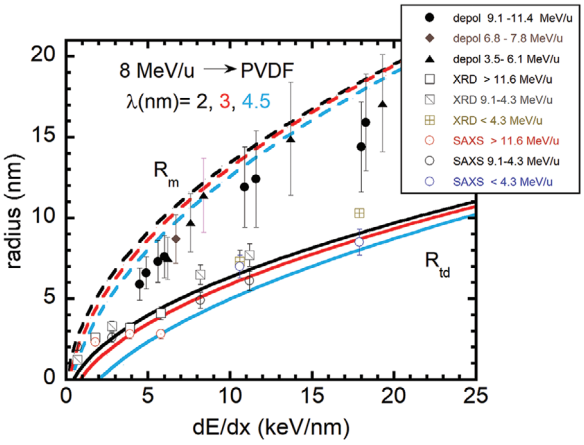

Figure 7. Radii of melting R_m (dashed lines) and thermal decomposition R_{td} (solid lines) induced in poly(vinylidene difluoride) (PVDF) as a function of energy loss at a fixed specific energy of 8 MeV u^{-1} derived from i-TS calculations. Activation energies of thermal decomposition of 0.173 eV at^{-1} and of melting of 0.062 eV at^{-1} were used. Curves for electron–phonon mean free path λ varying from 2 to 4.5 nm are shown. Closed symbols are experimental data of track radii extracted from depolarization of ion bombarded PVDF.[38] Open circles are track radii as deduced from small angle X-rays scattering (SAXS)[39] and open squares, deduced from X-ray diffraction (XRD).[12]

3.4. PVDF

Three sets of track size measurements in PVDF have been used for comparison with the i-TS calculations. One set encompasses the data from Hillenbrand et al., where effective ion track radii were deduced from ion beam depolarization of poled β-PVDF.[38] The others are XRD[12] and SAXS[39] investigations of irradiated α-PVDF. In those studies, the polymer was irradiated with ion beams with energies between 2 and 11.6 MeV u^{-1}. To compare with the experimental data, calculations were performed at a beam specific energy of 8 MeV u^{-1}. **Figure 7** displays the calculated track radii R_m where a molten phase is reached (E_m = 0.062 eV at^{-1}) and R_{td} where thermal decomposition occurs (E_d = 0.173 eV at^{-1}) together with the experimental results. As can be seen in Figure 7, the velocity effect is also small in this experimental data set.

Radii obtained from SAXS data follow closely the curve of thermal decomposition radii obtained from the i-TS, supporting the connection between the decrease in density in the ion track in a polymer and track pyrolysis. On the other hand, track radii derived from depolarization measurements are close to the radius of the molten phase in the i-TS calculations. As the residual polarization of PVDF is associated to the aligned chains in the crystalline regions, the depolarization of irradiated PVDF has been initially attributed to the loss of crystallinity.[38] However, the actual scenario is more complex because the amorphization radii derived from XRD, are significantly smaller than those from depolarization. That is, while depolarization is very sensitive to radiation damage and appears to be correlated to the appearance of a melt phase, there is no simple correlation between loss of crystallinity and ion induced melting.

The fact that depolarization and amorphization radii are different in PVDF suggests that the initial molten region in the tracks may partially recrystallize during cooling (reducing the apparent radius of amorphization from XRD), but this recrystallization cannot recover ferroelectricity. Indeed, the β-phase of PVDF does not recrystallize from the melt,[60] thus even if the poled PVDF chains partially recrystallize after the ion impact, neither the β-phase nor the preferential orientation of the dipoles responsible for ferroelectric behavior are recovered. The fact that radii of amorphization lie actually very close to the R_{td} curve suggests, in addition, the importance of bond-breaking in the loss of crystallinity induced by ion bombardment in PVDF.

Taken together the results on amorphization radii from PVDF and PET reveal the complexity of swift heavy ion induced amorphization in polymers, which may involve not only a physical phase change of molecular organization, but also chemical defects derived from radiolysis, such as chain scission and cross-linking. Swift heavy-ion-induced amorphization in polymers and its dependence on energy loss is a topic that deserves additional investigation, as experimental evidence is not only limited but also controversial.

4. Final Remarks

Track size calculations in polymers based on the inelastic thermal spike model were compared to experimental data deduced from a variety of experimental techniques, in a broad range of ion velocities and energy loss, where the electronic stopping is dominant. The i-TS matches reasonably well the overall evolution of track size as a function of electronic energy loss obtained from most experimental probes. For all polymers investigated, an electron–phonon mean free-path close to $\lambda = 3$ nm produces the best agreement between experiments and calculations. A more precise value of $\lambda = 3.2 \pm 0.3$ nm was deduced based on damage cross-section data acquired at constant ion velocity in PPS. This λ is within the expected values based on the band gap empirical rule for amorphous or disordered materials. Differently from most inorganic materials, where the appearance of the melt phase was found to be a suitable criterion for track formation, the activation energy for thermal degradation or pyrolysis[35] is the parameter that describes most of the observed track radii in the polymers studied here. Amorphization radii of the semicrystalline polymers are not directly correlated to melting in the spike. Only depolarization of β-PVDF appears to be correlated to the size of a molten zone.

As damage is not uniform across ion tracks in polymers, but rather displays a gradient from the highly carbonized core to the partially modified track edge, there are variations in the measured (and probe-dependent) track size for a given polymer that can only be accounted for by using different values of activation energies. This is evident in the case of PVDF where data probing both severe bond disruption and mass loss (e.g., SAXS) and more subtle order/disorder transitions (depolarization) are available. Such extremes follow either thermal decomposition or melting radii derived from the i-TS calculations. When track radius is deduced from IR spectroscopy, finer variations in effective damage radii associated with the destruction of different chemical groups are detectable. The values of these radii and their dependence on the energy loss of the ions are still well described by the i-TS model, if a specific activation energy is ascribed for each type of bond. The larger the stability or binding energy of a certain chemical group, the larger the activation energy obtained, as expected, and smaller is the corresponding track radius.

A few observations are needed concerning the low energy loss regime. In the calculated i-TS track radii, a threshold is always seen, because a minimum average energy per atom is required for a certain transition or phase change to occur. Here, we identified thermal decomposition (pyrolysis) as the basic reference to describe track size in polymers. It is linked to carbonization, material loss, and density change in the material. The electronic energy loss threshold of thermal decomposition deduced from the i-TS model (with $\lambda = 3$ nm) for all polymers investigated is close to or smaller than 1 keV nm^{-1} (0.9 keV nm^{-1} for PMMA with a beam of 3 MeV u^{-1}, 1.1 keV nm^{-1} for PET and PVDF with a beam of ≈5 MeV u^{-1}, ≈0.7 keV nm^{-1} for PPS with a beam of 0.6 MeV u^{-1}). The electronic energy loss threshold for the appearance of a molten phase as deduced from the i-TS model is 0.4 keV nm^{-1} for PVDF with a beam of ≈5 MeV u^{-1}, ≈0.2 keV nm^{-1} for PET with a beam between 1 and 11 MeV u^{-1}, ≈0.2 keV nm^{-1} for PPS with a beam of 0.6 MeV u^{-1} and ≈0.2 keV nm^{-1} for PMMA with a beam of ≈3 MeV u^{-1}. Such values of threshold are very low as compared to inorganic materials[21,24] showing the extreme sensitivity of polymers under heavy ion irradiation.

In the experiments, a threshold may or may not be observable, depending on the type of damage being probed. For example, cratering, i.e., the ejection of a volume of material in a single ion impact, is clearly a phenomenon which appears only at high ionization densities (to the best of our knowledge cratering in organic matter has never been reported at low energy loss). Bond-breaking, on the other hand, may still appear at very low electronic energy loss (below the threshold of track formation deduced from i-TS) due to the high sensitivity of polymers to single electronic excitation. We note that there is a lack of data on track size in polymers measured at low dE/dx. Filling this gap may help to distinguish the polymer transformations coming from single electronic excitations to the ones induced by the dense electronic excitation created along swift heavy ion tracks.

There are some stark differences in behavior among the polymers investigated, that calls for additional experiments. This is evident, for example, in the data related to ion beam induced amorphization. The XRD results of PVDF (which roughly follows i-TS thermal decomposition radii and also SAXS data) are distinctively different from PET (where radii scaling with dE/dx is unique and appears to be correlated to thermal degradation at low dE/dx but to melting at high energy loss). Moreover, again for PET, there are large variations in the damage cross-sections derived from IRAS bands associated with carbonization (what is unusual) and radii derived from SAXS are considerable smaller than those obtained for thermal degradation, in contrast to PVDF. This could be an indication that activation energies extracted from equilibrium conditions of thermal degradation used in the calculations may not be suitable for the highly energetic and transient track conditions. But still, they may also arise from uncertainties in the measurements and fittings of the raw data. Thus, polymeric materials need for sure an expanded and reliable data base with experiments designed to probe different types of damage performed under similar experimental conditions and in the largest range of energy loss possible keeping velocity fixed. This will allow a deeper and more robust understanding of the structure of tracks produced by swift heavy ions in this class of material.

Supporting Information

Supporting Information is available from the Wiley Online Library or from the author.

Acknowledgements

This work has been partially funded by the Brazilian Agency CAPES through the Institutional Internationalization Program (CAPES/PRINT) and by the National Institute of Science and Technology of Surface Engineering (INCT-INES-contract 465423/2014-0, CNPq). MRS received a CAPES fellowship, Finance Code 001. MT also thanks CAPES foundation for financial support for a one month stay at PUCRS, Brazil.

Conflict of Interest

The authors declare no conflict of interest.

Data Availability Statement

The data that support the findings of this study are available from the corresponding author upon reasonable request.

Keywords

inelastic thermal spike, ion tracks, polymers, radiation effects

Received: September 25, 2022
Revised: November 9, 2022
Published online: December 22, 2022

[1] A. Chapiro, *Radiat. Res., Suppl.* **1964**, *4*, 179.
[2] D. Fink, *Fundamentals of Ion-Irradiated Polymers*, Springer Berlin, Heidelberg **2004**.
[3] R. L. Fleischer, *MRS Bull.* **1995**, *20*, 17.
[4] R. Katz, R. Spohr, *Ion Tracks and Microtechnology: Principles and Applications*, Vol. *126*, Radiation Research Society, KS, USA **1991**.
[5] R. M. Papaléo, M. R. Silva, R. Leal, P. L. Grande, M. Roth, B. Schattat, G. Schiwietz, *Phys. Rev. Lett.* **2008**, *101*, 167601.
[6] R. M. Papaléo, R. Leal, C. Trautmann, E. M. Bringa, *Nucl. Instrum. Methods Phys. Res., Sect. B* **2003**, *206*, 7.
[7] P. Y. Apel, *Radiat. Phys. Chem.* **2019**, *159*, 25.
[8] I. V. Blonskaya, N. E. Lizunov, K. Olejniczak, O. L. Orelovich, Y. Yamauchi, M. E. Toimil-Molares, C. Trautmann, P. Y. Apel, *J. Membr. Sci.* **2021**, *618*, 118657.
[9] F. Studer, M. Hervieu, J.-M. Costantini, M. Toulemonde, *Nucl. Instrum. Methods Phys. Res., Sect. B* **1997**, *122*, 449.
[10] J. Jensen, A. Dunlop, S. Della-Negra, *Nucl. Instrum. Methods Phys. Res., Sect. B* **1998**, *141*, 753.
[11] D. Albrecht, P. Armbruster, R. Spohr, M. Roth, K. Schaupert, H. Stuhrmann, *Appl. Phys. A* **1985**, *37*, 37.
[12] V. Chailley, E. Balanzat, E. Dooryhee, *Nucl. Instrum. Methods Phys. Res., Sect. B* **1995**, *105*, 110.
[13] R. Papaléo, A. Hallén, B. Sundqvist, L. Farenzena, R. Livi, *Phys. Rev. B: Condens. Matter Mater. Phys.* **1996**, *53*, 2303.
[14] Z. Zhu, Y. Sun, C. Liu, J. Liu, Y. Jin, *Nucl. Instrum. Methods Phys. Res., Sect. B* **2002**, *193*, 271.
[15] Z. Zhu, C. Liu, Y. Sun, J. Liu, Y. Tang, Y. Jin, J. Du, *Nucl. Instrum. Methods Phys. Res., Sect. B* **2002**, *191*, 723.
[16] R. M. Papaléo, P. Demirev, J. Eriksson, P. Håkansson, B. U. R. Sundqvist, R. E. Johnson, *Phys. Rev. Lett.* **1996**, *77*, 667.
[17] P. Apel, A. Schulz, R. Spohr, C. Trautmann, V. Vutsadakis, *Nucl. Instrum. Methods Phys. Res., Sect. B* **1998**, *146*, 468.
[18] A. Adla, H. Fuess, C. Trautmann, *J. Polym. Sci., Part B: Polym. Phys.* **2003**, *41*, 2892.
[19] E. Balanzat, S. Bouffard, A. Le Moël, N. Betz, *Nucl. Instrum. Methods Phys. Res., Sect. B* **1994**, *91*, 140.
[20] N. Itoh, *Nucl. Instrum. Methods Phys. Res., Sect. B* **1996**, *116*, 33.
[21] C. Dufour, M. Toulemonde, in *Ion Beam Modification of Solids Ion-Solid Interaction and Radiation Damage*, Vol. *61* (Eds: W. Wesch, E. Wendler). Springer International Publishing, Cham **2016**, pp. 63–104.
[22] G. Szenes, *Phys. Rev. B* **1995**, *52*, 6154.
[23] G. Szenes, K. Havancsák, V. Skuratov, P. Hanák, L. Zsoldos, T. Ungár, *Nucl. Instrum. Methods Phys. Res., Sect. B* **2000**, *166–167*, 933.
[24] M. Toulemonde, C. Dufour, A. Meftah, E. Paumier, *Nucl. Instrum. Methods Phys. Res., Sect. B* **2000**, *166–167*, 903.
[25] M. Toulemonde, W. Assmann, C. Dufour, A. Meftah, F. Studer, C. Trautmann, in *Ion Beam Science: Solved and Unsolved Problems* (Ed: P. Sigmund), The Royal Danish Academy of Sciences and Letters, Copenhagen **2006**, pp. 263–292.
[26] A. Meftah, F. Brisard, J. M. Costantini, E. Dooryhee, M. Hage-Ali, M. Hervieu, J. P. Stoquert, F. Studer, M. Toulemonde, *Phys. Rev. B* **1994**, *49*, 12457.
[27] C. Dufour, Z. G. Wang, E. Paumier, M. Toulemonde, *Bull. Mater. Sci.* **1999**, *22*, 671.
[28] Z. G. Wang, C. Dufour, E. Paumier, M. Toulemonde, *J. Phys.: Condens. Matter* **1994**, *6*, 6733.
[29] A. Meftah, M. Djebara, N. Khalfaoui, M. Toulemonde, *Nucl. Instrum. Methods Phys. Res., Sect. B* **1998**, *146*, 431.
[30] A. Meftah, J. M. Costantini, N. Khalfaoui, S. Boudjadar, J. P. Stoquert, F. Studer, M. Toulemonde, *Nucl. Instrum. Methods Phys. Res., Sect. B* **2005**, *237*, 563.
[31] K. Awazu, X. Wang, M. Fujimaki, T. Komatsubara, T. Ikeda, Y. Ohki, *J. Appl. Phys.* **2006**, *100*, 044308.
[32] A. Kamarou, W. Wesch, E. Wendler, A. Undisz, M. Rettenmayr, *Phys. Rev. B: Condens. Matter Mater. Phys.* **2008**, *78*, 054111.
[33] C. S. Schnohr, P. Kluth, R. Giulian, D. J. Llewellyn, A. P. Byrne, D. J. Cookson, M. C. Ridgway, *Phys. Rev. B: Condens. Matter Mater. Phys.* **2010**, *81*, 075201.
[34] M. Sall, I. Monnet, F. Moisy, C. Grygiel, S. Jublot-Leclerc, S. Della–Negra, M. Toulemonde, E. Balanzat, *J. Mater. Sci.* **2015**, *50*, 5214.
[35] M. Skupinski, M. Toulemonde, M. Lindeberg, K. Hjort, *Nucl. Instrum. Methods Phys. Res., Sect. B* **2005**, *240*, 681.
[36] R. M. Papaléo, R. Thomaz, L. I. Gutierres, V. M. De Menezes, D. Severin, C. Trautmann, D. Tramontina, E. M. Bringa, P. L. Grande, *Phys. Rev. Lett.* **2015**, *114*, 118302.
[37] R. Thomaz, N. W. Lima, D. Teixeira, L. I. Gutierres, I. Alencar, C. Trautmann, P. L. Grande, R. M. Papaléo, *Curr. Appl. Phys.* **2021**, *32*, 91.
[38] J. Hillenbrand, N. Angert, H. L. Hartnagel, R. Neumann, *Nucl. Instrum. Methods Phys. Res., Sect. B* **1999**, *151*, 123.
[39] T. Steckenreiter, *Charkterisierung von Spuren Energiereicher Ionen in Polymeren*, Technische University, Darmstadt **1997**.
[40] P. Hermes, B. Danielzik, N. Fabricius, D. Linde, J. Kuhl, J. Heppner, B. Stritzker, A. Pospieszczyk, *Appl. Phys. A: Solids Surf.* **1986**, *39*, 9.
[41] B. Rethfeld, K. Sokolowski-Tinten, D. von der Linde, S. I. Anisimov, *Phys. Rev. B: Condens. Matter Mater. Phys.* **2002**, *65*, 092103.
[42] M. P. R. Waligórski, R. N. Hamm, R. Katz, *Int. J. Radiat. Appl. Instrum., Part D* **1986**, *11*, 309.
[43] J. F. Ziegler, M. D. Ziegler, J. P. Biersack, *Nucl. Instrum. Methods Phys. Res., Sect. B* **2010**, *268*, 1818.
[44] P. Guggillia, A. Chilvery, R. Powell, *Res. Rev.: J. Mater. Sci.* **2017**, *05*, 34.
[45] L. N. Ismail, H. Zulkefle, S. H. Herman, M. R. Mahmood, *Adv. Mater. Sci. Eng.* **2012**, *2012*, 6.
[46] K. Chikaoui, M. Izerrouken, M. Djebara, M. Abdesselam, *Radiat. Phys. Chem.* **2017**, *130*, 431.
[47] S. Asada, K. Seki, H. Inokuchi, *Chem. Phys. Lett.* **1986**, *130*, 155.
[48] W. N. Dos Santos, C. Y. Iguchi, R. Gregorio, *Polym. Test.* **2008**, *27*, 204.
[49] G. Botelho, S. Lanceros-Mendez, A. M. Gonçalves, V. Sencadas, J. G. Rocha, *J. Non-Cryst. Solids* **2008**, *354*, 72.
[50] T. Steinhaus, *Masters of Science Thesis*, The University of Maryland, **1999**.
[51] O. P. Korobeinichev, A. A. Paletsky, M. B. Gonchikzhapov, R. K. Glaznev, I. E. Gerasimov, Y. K. Naganovsky, I. K. Shundrina, A. Y. Snegirev, R. Vinu, *Thermochim. Acta* **2019**, *671*, 17.
[52] C. T. I. INC., TORELINA™ PPS Resin, https://www.toray.jp/plastics/en/torelina/technical/tec_013.html
[53] C. Teng, N. Mao, J. Liu, X. Tian, presented at Proc. Int. Conf. on Chemical, Material and Food Engineering, Kunming, Yunnan, China, July **2015**.
[54] A. A. Minakov, D. A. Mordvintsev, C. Schick, *Polymer* **2004**, *45*, 3755.
[55] P. Das, P. Tiwari, *Thermochim. Acta* **2019**, *679*, 178340.

[56] J. I. Scheinbeim, *Polymer Data Handbook*, Oxford University Press, Oxford **1999**.
[57] Mitsubishi, Hostaphan General Technical Data, https://www.m-petfilm.com/product-information/hostaphan-general-technical-data/#link35 (accessed: November, 2022).
[58] P. Apel, R. Spohr, C. Trautmann, V. Vutsadakis, *Radiat. Meas.* **1999**, *31*, 51.
[59] R. M. Papaléo, M. A. de Araújo, R. P. Livi, *Nucl. Instrum. Methods Phys. Res., Sect. B* **1992**, *65*, 442.
[60] A. J. Lovinger, *Science* **1983**, *220*, 1115.